

RESEARCH ARTICLE

10.1002/2016WR020205

Isolating roughness scales of gravel-bed patches

Stephane Bertin¹ , Jane Groom¹ , and Heide Friedrich¹

¹Department of Civil and Environmental Engineering, University of Auckland, Auckland, New Zealand

Key Points:

- Moving-window detrending allows separate examination of grain and bedform roughness contained in patch-scale DEMs
- There is a strong correlation between coarse surface sediment size and vertical roughness at both the grain and bedform scale
- Linear relationships connect the vertical roughness of gravel-bed patches to grain and bedform vertical roughness

Supporting Information:

- Supporting Information S1

Correspondence to:

S. Bertin,
s.bertin@gmail.com

Citation:

Bertin, S., J. Groom, and H. Friedrich (2017), Isolating roughness scales of gravel-bed patches, *Water Resour. Res.*, 53, 6841–6856, doi:10.1002/2016WR020205.

Received 29 NOV 2016

Accepted 20 JUL 2017

Accepted article online 26 JUL 2017

Published online 14 AUG 2017

Abstract There is a growing consensus that gravel-bed roughness should be parameterized based on bed-surface topography, not only sediment size. One benefit is the possible identification of various spatial scales of surface roughness and evaluation of their respective contributions to flow resistance (and also to bedload transport). The absence of relationships between roughness at the different scales is apparent in previous work, which currently limits roughness parameterization from topography and application in flow modeling. This study examines the use of moving-window detrending on gravel-bed digital elevation models (DEMs) for isolating roughness scales and their respective signatures. A large data set of 35 water-worked gravel-bed patches from both the laboratory and the field was used for the analysis. The measured bed topography was separated into two distinct DEMs: one representing grains, the other representing small bedforms. For all DEMs, bed-elevation parameters measuring vertical roughness, imbrication, and spatial correlations were determined. Our results show distinct topographic signatures between grain and bedform DEMs. We show strong positive linear relationships between grain vertical roughness and the size of the bed-surface material. Surface sediment arrangement also determined bedform shape, with groupings of coarse sediment forming humps on the surface, and finer sediment sheltered in hollows. Patch-scale vertical roughness could not be estimated simply as the sum of grain and bedform vertical roughness. Instead, our results suggest weighted summation and the existence of universal weighting coefficients. Practical applications for studies on gravel-bed roughness and flow modeling using DEMs are discussed.

1. Introduction

Observations of water-worked gravel beds and their microtopography, for example embodied in patch-scale high-resolution digital elevation models (DEMs), show the superposition of reliefs due to the arrangement of sediment grains onto low-amplitude bedforms [e.g., Pender *et al.*, 2001; Marion *et al.*, 2003; Powell *et al.*, 2016]. There is no consensus on the origin of these gravel bedforms, whether they are dynamic features, such as bedload sheets [Pender *et al.*, 2001], or bed undulations forming in tandem with a coarse surface layer during armoring [Powell *et al.*, 2016]. Bedforms in gravel-bed streams are nevertheless important controls on flow energy dissipation [Griffiths, 1989] and bed stability [Church *et al.*, 1998].

Using structure/autocorrelation functions to analyze correlations in gravel-bed elevations, previous research identified various scales of surface roughness [e.g., Robert, 1988, 1991; Butler *et al.*, 2001]. That is, the roughness signature (e.g., the range of elevations and other topographic properties) of gravel beds varies with the spatial scale at which the signature occurs. Subgrain roughness was referred to as the surface properties of a grain, while the size and orientation of individual grains was related to grain roughness [Butler *et al.*, 2001], which is the roughness due to the ensemble of the grains. Sediment grains may group together to form small structures, such as cluster microforms [Brayshaw, 1985]. This can represent a third intermediate roughness scale. Roughness characterized by the arrangement of features several times the size of the largest grains on the riverbed relates to bedform (also called form or macro) roughness [Robert, 1988, 1991]. The difficulty to make a clear differentiation between roughness scales is nevertheless evident from previous work. One reason is analytical, with the methods used often requiring a degree of judgment to associate observations of a transition between roughness scales (e.g., a break in slope in structure functions) to the corresponding bed features [Clifford *et al.*, 1992; Butler *et al.*, 2001].

Despite recent developments in remote sensing [e.g., Coleman *et al.*, 2011; Tarolli, 2014], measuring riverbed topography in a range of practical situations remains challenging. This is because of the need for high-resolution and accurate data to resolve individual grain arrangement, and challenging measurement environments restricting efficient and effective data recording of features such as submerged topographies.

Even when measurement allows, using high-resolution DEMs in flow modeling studies over rough beds is still hindered by the necessary trade-off between spatial extent and sampling resolution imposed by finite computing and time resources [Lane *et al.*, 2002]. It is however important to account for the small-scale riverbed topography in order to correctly characterize flow variability and turbulence [Hardy *et al.*, 2009]. Data from grain size and general fractal properties of water-worked gravel surfaces have been used for subgrid-scale roughness parameterization (i.e., the reconstruction of microtopography) [Casas *et al.*, 2010], due to a lack of knowledge on the relationships between roughness at the different scales for gravel beds.

The adoption of integral (i.e., nonpartitioned) measures of bed roughness is another example for which it is important to explicitly account for the various spatial scales of roughness. For instance, knowing the standard deviation of bed elevations (σ_z), herein called vertical roughness, improves flow resistance calculations over rough beds, replacing roughness parameters based on sediment size [Smart *et al.*, 2002; Aberle and Smart, 2003; Noss and Lorke, 2016]. Vertical roughness was initially calculated from DEMs after removal (i.e., detrending) of bed undulations larger than grain roughness, for example bedform roughness [Smart *et al.*, 2002]. However, other studies calculated σ_z from the bed topography without prior detrending of bedform roughness [Aberle and Nikora, 2006; Hodge *et al.*, 2009]. This makes comparing bed variability and roughness between studies difficult, as the quantities measured and subsequently compared do not necessarily encompass the same scales of surface roughness.

In this paper, we examine relationships between low-amplitude bed undulations developed by water working (which we call bedforms) and the relief created by sediment grains' arrangement. We discuss what our results mean for gravel-bed roughness parameterization and practical applications. A large data set, consisting of 35 water-worked gravel-bed patches from both the laboratory (17 DEMs) and the field (18 DEMs), was used for the analysis. Thus, it is expected that results provide general findings applicable for both controlled and uncontrolled gravel-bed environments. Moving-window detrending was applied to each of the 35 DEMs to separate bed undulations from the topography due to the grains, leading to two distinct surfaces: one representing grains (which we call the "grain DEMs"), the other representing small bedforms (called "the bedform DEMs"). The novelty of the study is the separate examination of grain and bedform roughness isolated from DEMs. The primary objectives are to (1) test moving-window detrending as a means to isolate roughness scales from DEMs; (2) determine roughness signatures for both grain and bedform DEMs using surface metrics commonly used for gravel beds; and (3) examine interrelationships between grain and bedform roughness and their formative controls.

2. Methods

2.1. Gravel-Bed Patches and the Data Examined

The authors collected DEMs and measured grain-size distributions (GSDs) for 21 gravel patches. Fourteen DEMs collected by others using a different measurement technique and already presented elsewhere [Smart *et al.*, 2004; Aberle and Nikora, 2006] are also examined. All DEMs satisfied the precondition of high-resolution data necessary for grain roughness analysis, as evidenced by a small DEM grid spacing compared to the size of the bed-surface material (Table 1).

Characteristic grain sizes of the bed surface (i.e., armor layer, but not the subsurface) are presented in Table 1 for all data used for analysis. GSDs and their percentiles (e.g., D_{50A} , the grain size for which 50% of the bed-surface material is smaller) were all determined using Fehr's [1987] line-by-number method, hence facilitating comparisons between data sets. Image-based methods applying Fehr's line-by-number method for the results analysis [e.g., Detert and Weitbrecht, 2012] were used by the authors and by Aberle and Nikora [2006], while Smart *et al.* [2004] manually sampled the bed surface of the Waimakariri River. The ground resolution of the imagery data collected by the authors was in the range 0.17–0.21 mm/pixel. According to Graham *et al.* [2010], this could automatically resolve grains with a b-axis larger than 3.9–4.9 mm (corresponding to 23 pixels in the images). Aberle and Nikora [2006] and Smart *et al.* [2004] do not present information on the minimum grain size detected by their measurements.

Data collection by the authors was made with digital photogrammetry [Bertin *et al.*, 2015]. A pair of Nikon D5100 cameras (16.4 Mpixel, 23.6×15.6 mm² sensor size), with Nikkor 20 mm lenses, was installed in stereo (horizontal baseline distance between cameras between 0.25 and 0.3 m) vertically (i.e., both cameras looking down) above the gravel surfaces. The photogrammetric technique employed herein to obtain

Table 1. Data Summary of Flow Conditions (Experimental Beds Only), Surface Sediment, and Topography^a

	Flow Conditions		Surface Sediment				Surface Topography					
	Sf	τ^*	D _{50A} (mm)	D _{84A} (mm)	D _{90A} (mm)	D _{hu} /D _{ho}	Size/D _{50A}	Grid (mm)	σ_z (mm)	$\sigma_{z,G}$ (mm)	$\sigma_{z,B}$ (mm)	I(0°)
Field 1			18.7	25.0	27.3	1.28	35 × 32	1 × 1	6.1	4.0	4.1	0.067
Field 2			47.2	89.0	104.7	1.47	13 × 13	1 × 1	18.3	14.2	12.0	0.115
Field 3			19.4	38.1	47.7	1.19	26 × 26	1 × 1	8.9	6.1	5.0	0.057
B1P01			18.2	31.2	35.7	1.24	80 × 25	1 × 1	6.1	4.1	3.9	0.059
B1P03A			20.0	33.6	37.4	1.14	43 × 22	1 × 1	6.4	5.0	3.1	0.038
B1P03B			20.0	33.6	37.4	1.30	25 × 22	1 × 1	6.5	4.6	3.9	0.034
B1P04			23.4	48.2	58.0	1.52	37 × 21	1 × 1	9.7	7.2	5.6	0.059
B1P05			24.0	52.3	64.4	1.41	71 × 17	1 × 1	10.5	6.3	7.0	0.071
B1P06A			25.3	49.8	54.5	1.32	31 × 17	1 × 1	8.9	6.5	4.7	0.084
B1P07A			22.2	42.9	50.9	1.38	47 × 13	1 × 1	8.1	6.4	4.5	0.063
B1P08			18.3	34.4	40.2	1.35	101 × 21	1 × 1	6.4	4.1	4.3	0.028
B1P09			19.7	37.5	46.2	1.14	83 × 18	1 × 1	7.5	4.0	6.0	0.027
B1P10			22.7	48.0	56.1	1.42	64 × 17	1 × 1	10.0	6.6	6.4	0.052
B1P11			16.5	28.2	32.8	1.18	92 × 25	1 × 1	5.6	3.5	4.0	0.024
B1P12			15.0	27.3	32.2	1.14	36 × 35	1 × 1	4.9	2.7	3.8	0.015
B1P13			18.5	34.2	40.7	1.36	62 × 24	1 × 1	6.7	4.7	4.1	0.021
B2P04			23.1	45.8	51.8	1.48	24 × 23	1 × 1	11.7	7.4	7.1	0.029
Sed1_Q1	0.005	0.044	18.0	23.0	25.0	1.10	47 × 19	1 × 1	3.7	2.8	2.0	0.016
Sed1_Q2	0.005	0.050	18.5	24.5	27.0	1.04	46 × 19	1 × 1	4.3	3.1	2.5	0.025
Sed2_Q1	0.005	0.040	18.0	24.0	26.0	0.93	49 × 20	1 × 1	4.9	3.5	3.2	−0.01
Sed2_Q2	0.005	0.046	18.5	26.0	28.0	0.99	44 × 18	1 × 1	5.0	3.5	3.1	0.051
I_Qc250a	0.0027	0.100	19.5	47.5	52.8 ^b	1.37	122 × 37	1 × 4	11.0	7.9	7.7	0.068
I_Qc250b	0.0027	0.102	19.6	48.4	53.8 ^b	1.39	121 × 37	1 × 4	10.6	7.5	6.6	0.078
I_Qc120	0.0027	0.062	11.1	27.2	30.2 ^b	1.07	215 × 65	1 × 4	4.9	3.4	3.3	0.054
I_Qc180	0.0027	0.074	13.6	28.7	31.9 ^b	1.16	175 × 53	1 × 4	6.5	4.2	4.6	0.079
I_Qc220	0.0027	0.083	18.4	44.4	49.3 ^b	1.21	129 × 39	1 × 4	8.6	5.9	5.5	0.076
II_Qc120	0.0027	0.057	11.3	24.7	27.4 ^b	1.07	211 × 63	1 × 4	6.1	3.1	5.0	0.083
II_Qc180	0.0027	0.075	15.3	32.4	36.0 ^b	1.15	155 × 47	1 × 4	7.6	4.9	5.2	0.072
II_Qc220	0.001	0.089	17.7	47.4	52.7 ^b	1.23	134 × 40	1 × 4	8.4	6.1	5.2	0.077
III_Qc120	0.01	0.075	23.5	44.0	48.9 ^b	1.11	101 × 30	1 × 4	10.2	7.0	6.7	0.099
III_Qc180	0.01	0.095	25.0	48.8	54.2 ^b	1.23	95 × 29	1 × 4	13.3	8.9	8.7	0.133
III_Qc240	0.01	0.086	25.3	49.8	55.3 ^b	1.34	94 × 28	1 × 4	13.1	9.6	7.4	0.133
IV_Qc120	0.001		9.1	23.1	25.7 ^b	1.07	263 × 79	1 × 4	4.6	2.7	3.5	0.081
IV_Qc180	0.001		11.2	29.0	32.2 ^b	1.26	212 × 64	1 × 4	6.2	3.8	4.5	0.086
Waimakariri			47.0	78.3 ^b	87.0	1.20	19 × 13	2 × 2	16.2	13.1	7.5	0.139

^aSf, flume slope; τ^* , Shields stress based on bulk mixture D₅₀; D_{50A}, D_{84A}, D_{90A}, bed-surface characteristic grain sizes; D_{hu}/D_{ho} corresponds to the ratio of D_{84A} calculated (relationship presented in Figure 3e) on bed humps and hollows, separately; size/D_{50A} is DEM size, downstream × transverse, normalized by D_{50A}; grid is DEM grid spacing, downstream × transverse; σ_z , standard deviation of measured bed elevations; $\sigma_{z,G}$, standard deviation of bed elevations for the grain DEMs; $\sigma_{z,B}$, standard deviation of bed elevations for the bedform DEMs; I(0°) is inclination index measuring grain imbrication parallel to the flow direction on the grain DEMs.

^bThe following relation was used: $0.9 \times D_{90A} = D_{84A}$.

DEMs from stereo photographs (i.e., two overlapping images) consists of (i) in situ calibration, using the method of Zhang [1998], included in Bouquet's [2010] open-access calibration toolbox for Matlab®, which requires several stereo photographs of a planar chequerboard to determine both intrinsic (i.e., camera) and extrinsic (i.e., setup) calibration parameters; (ii) using the calibration data to accurately rectify (aim is for a mean rectification error <0.5 pixel and maximum error <1 pixel throughout the imaging area) stereo photographs of the gravel beds to epipolar geometry, whereby corresponding pixels between overlapping images are ideally on a same scanline; and (iii) scanline-based pixel-to-pixel stereo matching using Gimel'farb's [2002] symmetric dynamic programming stereo (SDPS) algorithm, providing both point cloud data and ortho-images. Using the SDPS, occluded points (i.e., which cannot be seen in one or the two images) are interpolated based on the assumption of a continuous surface, leaving no voids. The careful design of the measurement setup (e.g., adjusting the baseline and the camera height to the relief of the surface) helps to minimize occlusions [Lane et al., 2001; Bertin et al., 2015]. However, determining the proportion of occluded points was not possible. Subsequently, point clouds were transformed into raster DEMs with final grid spacing equal to 1 mm and rotated to be aligned with the surface-forming flow direction. While flow direction identification is straightforward for laboratory surfaces, the flow direction for field data was determined by eye from observations of channel shape and grain imbrication [Laronne and Carson, 1976; Millane et al., 2006; Bertin and Friedrich, 2016]. Rigorous quality assurance testing was applied to our photogrammetric DEMs to ensure representative surface metrics with minimum impact from measurement errors. For

instance, DEM accuracy (here the mean absolute error between measurements and true values) was estimated using a 3-D-printed gravel-bed model ($296 \times 184 \text{ mm}^2$) to be ~ 0.4 and ~ 0.7 mm in the laboratory and in the field, respectively [Bertin et al., 2014; Bertin and Friedrich, 2016].

Using the photogrammetric method described above, four DEMs were collected in a laboratory flume (glass-sided, 19 m long, 0.45 m wide, and 0.5 m deep, with a slope set at 0.5%) for a study on stable fluvial armors. The armored beds were obtained from water-working two sediment mixtures (called Sed1 and Sed2) at two successive discharges ($Q_1 = 67 \text{ L/s}$ and $Q_2 = 84 \text{ L/s}$; see Table 1 for details of the formative Shields stress) until the rate of sediment transport dropped to practically zero. Both sediment mixtures were prepared from distinct slightly bimodal alluvial sediments (15% sand and 85% gravel, and 9% sand and 91% gravel, respectively), with grain size ranging from 0.7 to 35 mm, a D_{50} of 8.4 and 9.2 mm and a sorting coefficient of 1.5 and 1.2 [Folk and Ward, 1957] for Sed1 and Sed2, respectively. The tests were performed under conditions of sediment starvation (i.e., no sediment feeding). DEMs were obtained by merging three overlapping DEMs, with a final areal coverage of $1 \times 0.45 \text{ m}^2$ (downstream \times transverse). Under laboratory conditions, measured elevations were characterized by a horizontal and a vertical resolution of 0.17 and 0.36 mm, respectively. To minimize flume wall influence on the bed properties measured, DEMs were cropped to $0.8 \times 0.35 \text{ m}^2$ before analysis. The armors formed at the discharge Q_1 were measured through-water, to avoid draining the flume during the tests. At the end of the tests, the armors formed at the discharge Q_2 were measured through water and in air. Both measurements gave similar results, exemplified by a mean absolute difference between DEM points ~ 0.7 mm.

The authors also measured gravel patches from the Whakatiwai River, a small gravel-bed stream located in New Zealand North Island, in August 2014 (3 DEMs, called Field 1–3 presented in Bertin and Friedrich [2016]) and in August 2016 (14 DEMs). Patches from exposed gravel bars were selected for measurements, covering a range of sediment size and surface structure. DEMs obtained during the first field campaign covered areas ranging from $0.5 \times 0.5 \text{ m}^2$ to $0.63 \times 0.63 \text{ m}^2$, with horizontal and vertical resolutions of 0.21 and 0.53 mm, respectively. During the second field campaign, larger DEMs were obtained by merging overlapping DEMs (as in Bertin et al. [2016]), which resulted in merged DEMs of size up to $1.851 \times 0.378 \text{ m}^2$ with horizontal and vertical resolutions of 0.19 and 0.47 mm, respectively. Some patches contained scattered vegetation. In this case, DEMs were cropped to allow the study of nonvegetated areas only and DEMs were annotated with letters to distinguish them from the raw DEMs.

Data collected from stable armors formed in a laboratory flume and presented in Aberle and Nikora [2006] represent 13 of the DEMs analyzed hereafter, provided to the authors. Experimental conditions (formative Shields stress, bed slope, and discharge in L/s contained in the DEM name) are presented in Table 1. DEMs were measured by moving a laser displacement meter (downstream and transverse point spacing of 1 and 4 mm, respectively) over an area of $2.4 \times 0.716 \text{ m}^2$ with a stated vertical accuracy of 0.1 mm.

Another field DEM used in the study was collected from the Waimakariri River in New Zealand South Island [Smart et al., 2004; Millane et al., 2006], using a hand-held laser scanner swept across the exposed gravel patch (area $0.89 \times 0.618 \text{ m}^2$). The stated horizontal resolution and vertical accuracy is approximately 1 mm. The DEM provided to the authors had a grid spacing of 2 mm.

2.2. Isolating Grain and Bedform Roughness From DEMs

All DEMs available for the study were first detrended to remove planar trends using a least squares fit procedure. The planar trends removed from the data can originate from bed/flume slope and from the orientation of the measurement device with respect to the bed surface. The DEMs after linear detrending are hereafter referred to as the “measured DEMs.” Second, moving-window detrending [e.g., Smart et al., 2002; Powell et al., 2016] was applied to the measured DEMs to isolate any bed undulations (e.g., humps and hollows on the surface) larger than the biggest individual particles. Following the method presented in Smart et al. [2002], a trend surface is fitted to a regular grid with point spacing equal to $1.25D_{90A}$, and the elevations of grid points are determined by averaging measured elevations within a circle with a diameter of $2.5D_{90A}$ centered on the grid point. Bubic spline interpolation is used to interpolate between trend surface grid points at the location of the measured DEM points. The interpolated surfaces represent the “bedform DEMs,” and subtracting these surfaces from the measured DEMs isolates the topography due to the sediment grains, hence produces the “grain DEMs.” The filter diameter used for moving-window detrending controls the size of the features retained in the grain and bedform DEMs. A correct setting is thus critical for

effective separation of the two roughness scales. The effect of changing the filter diameter is evaluated in section 4.1. Finally, all *measured*, *grain*, and *bedform* DEMs were normalized to have a zero-mean bed level. Given planar trends were removed during detrending, DEMs were thus free of first-order nonstationarity, allowing for the use of bed-elevation structure functions for the analysis [Hodge *et al.*, 2009].

2.3. Data Analysis

To characterize differences between grain and bedform roughness, and to illustrate eventual relationships, the same analysis was performed for all *measured*, *grain*, and *bedform* DEMs. The analysis first focused on simple properties of the DEMs, such as the standard deviation of bed elevations, σ_z . This is a robust measure of bed vertical roughness, quantifying the variability of bed elevations, used in a number of studies, at scales ranging from a gravel patch to a floodplain [e.g., Nikora *et al.*, 1998; Scown *et al.*, 2015].

Second-order structure functions of bed elevations [Nikora *et al.*, 1998; Butler *et al.*, 2001] were measured for all DEMs to quantify correlations in bed elevations at different spatial lags and in different directions (see supporting information). When plotted in 2-D, structure functions enable easy identification of the length and spatial arrangement of features on the surface layer. The maximum spatial lags used for computations were set to approximately half the DEM size, being always larger than the coarsest sediment grain on the surface.

Gravel-bed patches were also assessed in terms of the inclination index measured in the flow direction, $I(0^\circ)$, following the method presented by Millane *et al.* [2006]. The inclination index was computed using a lag distance between elevations equal to the grid spacing, and slopes with a value between ± 0.01 were removed from the analysis to leave only slopes with a definite positive or negative value. A positive inclination index reflects the predominance of positive DEM cell slopes, which here are counted as bed elevations increasing downstream. Given prior removal of the general bed inclination with linear detrending, a positive inclination index is characteristic of grain imbrication. The importance of detrending before using the inclination index is mentioned in Millane *et al.* [2006]. However, it is not clear if bedforms should be filtered in addition to planar trends. The results presented herein enable examination of the effect of detrending on the inclination index.

A moving-window analysis technique (not to be confused with moving-window detrending used for isolating roughness scales) was used to quantify the spatial variations in roughness parameters within DEMs. In this case, DEM properties were calculated over moving square windows of size proportional to the surface material D_{50A} . A large overlap between moving windows (95% overlap) enabled robust quantification of spatial variability, even at large window sizes.

3. Results

3.1. Isolating Roughness Scales of Gravel-Bed Patches

Figure 1 presents two gravel-bed patches collected by the authors and analyzed in this study. The two patches serve as examples to demonstrate patterns observed for all. The evidence that patterns persist for the other patches is presented later on (e.g., Figures 2–5). The first patch we present was measured in a laboratory flume, while the other was collected in the field. The superposition of grain topography (Figures 1c and 1d) and low-amplitude bed undulations (Figures 1e and 1f) is easily evidenced in both of them. Resulting from roughness scale separation, grain DEMs have a flat mean-bed level with high-frequency irregularities due to the grains (Figures 1c and 1d), while bedform DEMs show smooth topographies, which represent the lower-frequency bed undulations (Figures 1e and 1f). Visually, bed undulations appear to depend on coarse sediment arrangement on the surface. Humps are generally associated with groupings of coarse particles into small-scale structures such as clusters, lines, and stone cells, whereas smaller particles are confined in shelters formed by hollows. This visual assertion, particularly strongly evident in the laboratory DEM (Figures 1a, 1c, and 1e), was demonstrated quantitatively for all DEMs, with results presented in Figure 4.

Across all gravel-bed patches studied, the range of bed elevations due to sediment grains accounts for 87% of the total range of bed elevations, on average (standard deviation $\sigma = 15\%$, $n = 35$), whereas the range of bed elevations due to bedforms represents on average 65% ($\sigma = 23\%$) of the total range of bed elevations. Gravel-bed topography is not the net summation of grain and bedform topographies, rather a combination

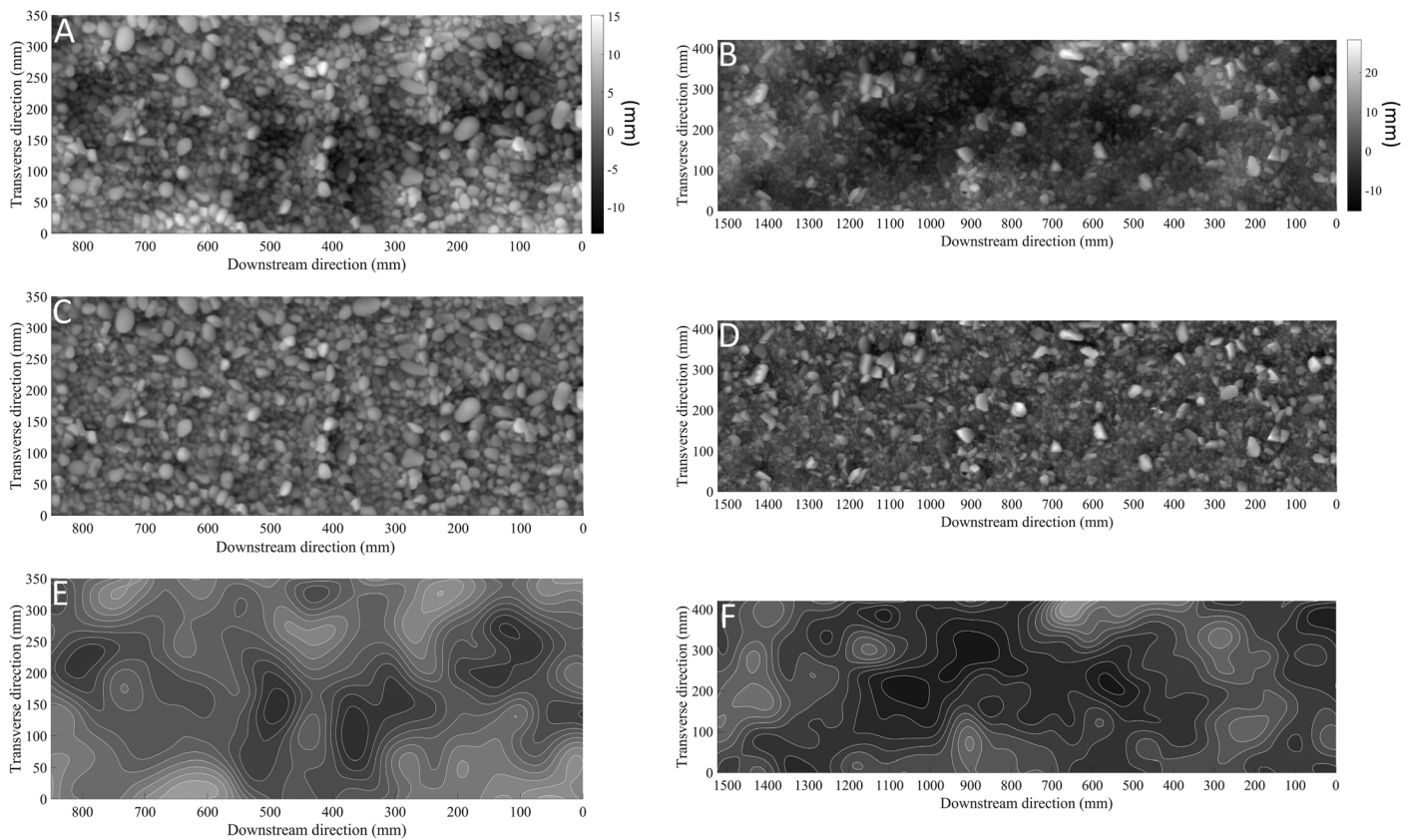


Figure 1. Example measured DEMs representing the microtopography of gravel-bed patches collected by the authors over experimentally (A, Sed1_Q2) and naturally (B, B1P11) water-worked surfaces, showing the superposition of two distinct topographic signatures. Planar trends representing a combination of bed slope and setup misalignment were removed from the measured DEMs (a, b). Following moving-window detrending on the measured DEMs with a filter diameter of $2.5D_{90A}$, the grain DEMs (c, d) show the topography due to the grains alone, while the bedform DEMs (e, f) show the underlying bed undulations. Elevation is represented as gradients of grays and vertical scaling is same for DEMs of the same origin.

of the two. One reason is the moving-window detrending technique, which averages out the bed topography locally. Thus, the trend ascribed to bedforms passes through the mean bed level for each window, not underneath the grain topography. Observation of the bedform DEMs (Figures 1e and 1f), showing the location of the most prominent grain structures, makes clear that the contributions of grain and bedform roughness are not entirely separate.

3.2. Vertical Roughness and the Distinct Signatures for Grains and Bedforms

In Figure 2, we present results obtained using the moving-window analysis technique. Not all results of the 35 DEMs analyzed can be presented. We therefore chose to highlight visual results for four representative DEMs, allowing the identification of consistent patterns. As shown in Table 1, the selection incorporates data from all sources available for the study, data collected from both the laboratory and the field, and the selection covers the largest possible range of surface sediment size ($D_{50A} = 9.1$ to 47.0 mm). The latter is likely indicative of a range of formative flow conditions. Figure 2 shows that the standard deviation of bed elevations (σ_z), representing vertical roughness, measured over moving square windows of size proportional to the sediment surface D_{50A} , varies across a gravel patch and that a sufficient window (hence DEM) size is necessary to obtain measures of σ_z representative of the surface. This is shown by large variability and unstable median values at small window sizes, until it plateaus out. Robust measures of vertical roughness for the grain DEMs (i.e., $\sigma_{z,G}$) are attained for square window sizes above $\sim(12-18D_{50A})^2$. Larger DEMs are necessary to determine robust measures of bedform signature representative of the surface. Indeed, σ_z measured over the bedform DEMs (i.e., $\sigma_{z,B}$) has a wider range (evidenced by unstable median values and more variability) than σ_z measured over the grain DEMs at similar window sizes, because of different scales of roughness measured. Another observation from Figure 2 is that σ_z of the measured DEMs is different from the sum of σ_z obtained separately from the grain DEMs and the bedform DEMs (i.e., $\sigma_z \neq \sigma_{z,G} + \sigma_{z,B}$),

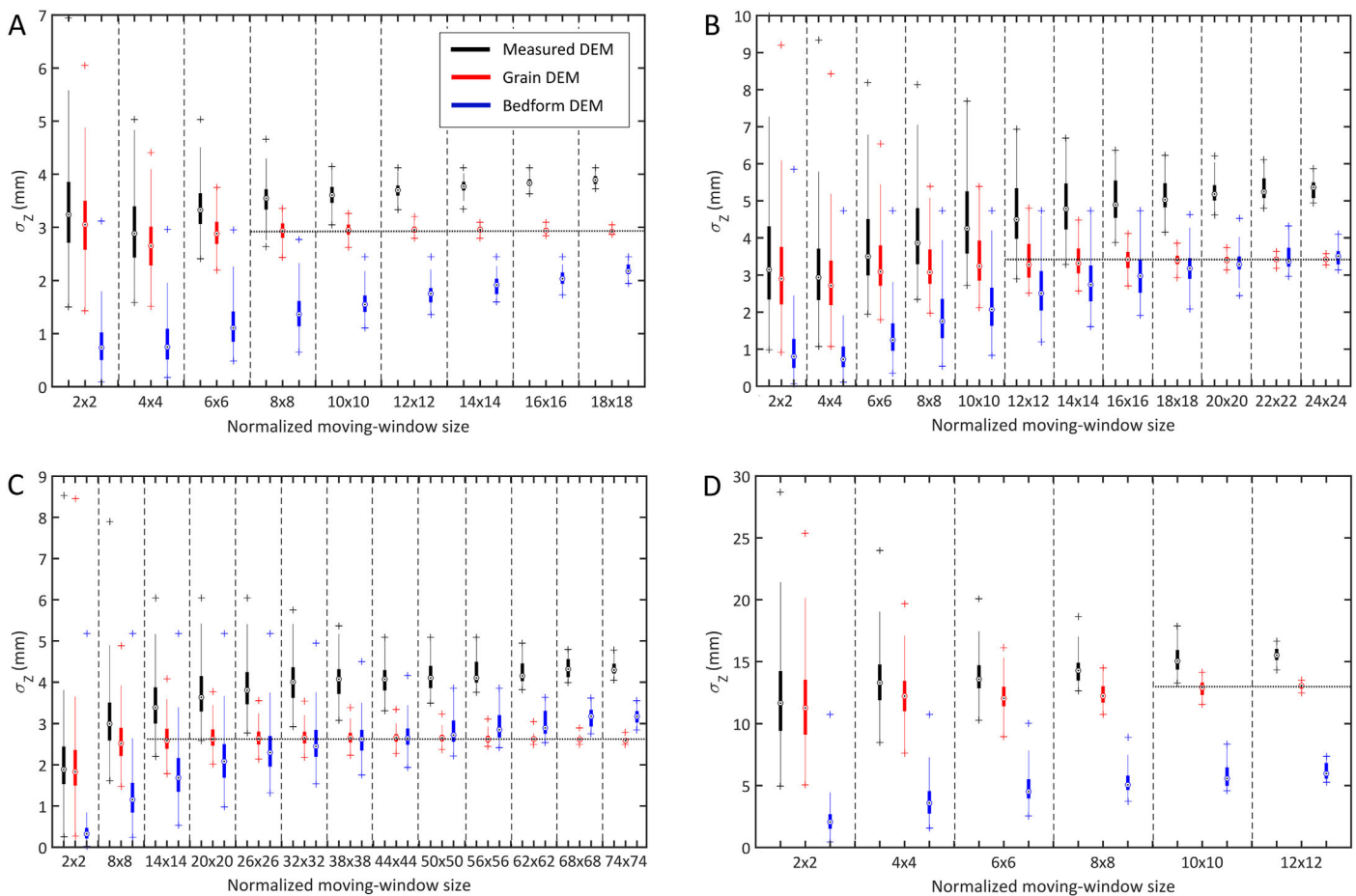


Figure 2. Moving-window analysis examining spatial variations in standard deviation of bed elevations for the measured (σ_z), grain ($\sigma_{z,G}$), and bedform ($\sigma_{z,B}$) DEMs, for (a) Sed1_Q2; (b) B1P11; (c) IV_Qc120 [Aberle and Nikora, 2006]; and (d) Waimakariri [Smart et al., 2004]. X axis is moving-window size normalized in both directions by D_{50A} . Boxes represent 25th–75th percentile range, circles within boxes indicate median, lines above and below boxes show the range of extreme values which are not considered outliers (i.e., values within 1.5 of the interquartile range) and crosses indicate minimum and maximum values (outliers were removed for clarity). Horizontal lines were added to help visualize the plateauing in grain vertical roughness with window size increases.

which statistically, indicates a correlation between $\sigma_{z,G}$ and $\sigma_{z,B}$. The inadequacy of summing individual roughness components to derive the total roughness of the bed has been observed in previous work and explained by interaction effects between roughness scales [e.g., Hey, 1988; Wilcox et al., 2006]. The analogy with the present study is limited however, as previous work derived roughness from flow resistance models, not from the bed topography.

3.3. Relationships Between Roughness at the Different Scales

Scatterplots between vertical roughness (σ_z) and characteristic grain sizes of the bed-surface material are presented in Figure 3 for the 35 DEMs. For the purpose of comparisons between variables subject to errors, linear functional relationships [Mark and Church, 1977], which minimize the sums of the squared perpendicular distances from the data points to the lines, were used in replacement of the usual (least squares) regression lines. The relationships developed are stronger as percentiles of the bed-surface grain-size distribution increase, as indicated by higher Pearson coefficients of determination (R^2). This suggests that for the patches examined, the size of the coarse surface sediment is a better indicator of the patch topography. This observation needs to be taken with caution, however, as the authors' and Smart et al.'s [2004] D_{50A} values appear systematically higher than the values measured by Aberle and Nikora [2006], for a given σ_z (Figures 3a–3c). This appearance of an operator effect in the collapsed data set may well result from differences measuring surface sediment size between studies (e.g., the minimum grain size sampled), and this may have an effect on the R^2 values obtained with D_{50A} . There is no appearance of an operator effect for D_{84A} and D_{90A} . Despite the caveat, relationships are stronger when sediment size is compared to $\sigma_{z,G}$ for the

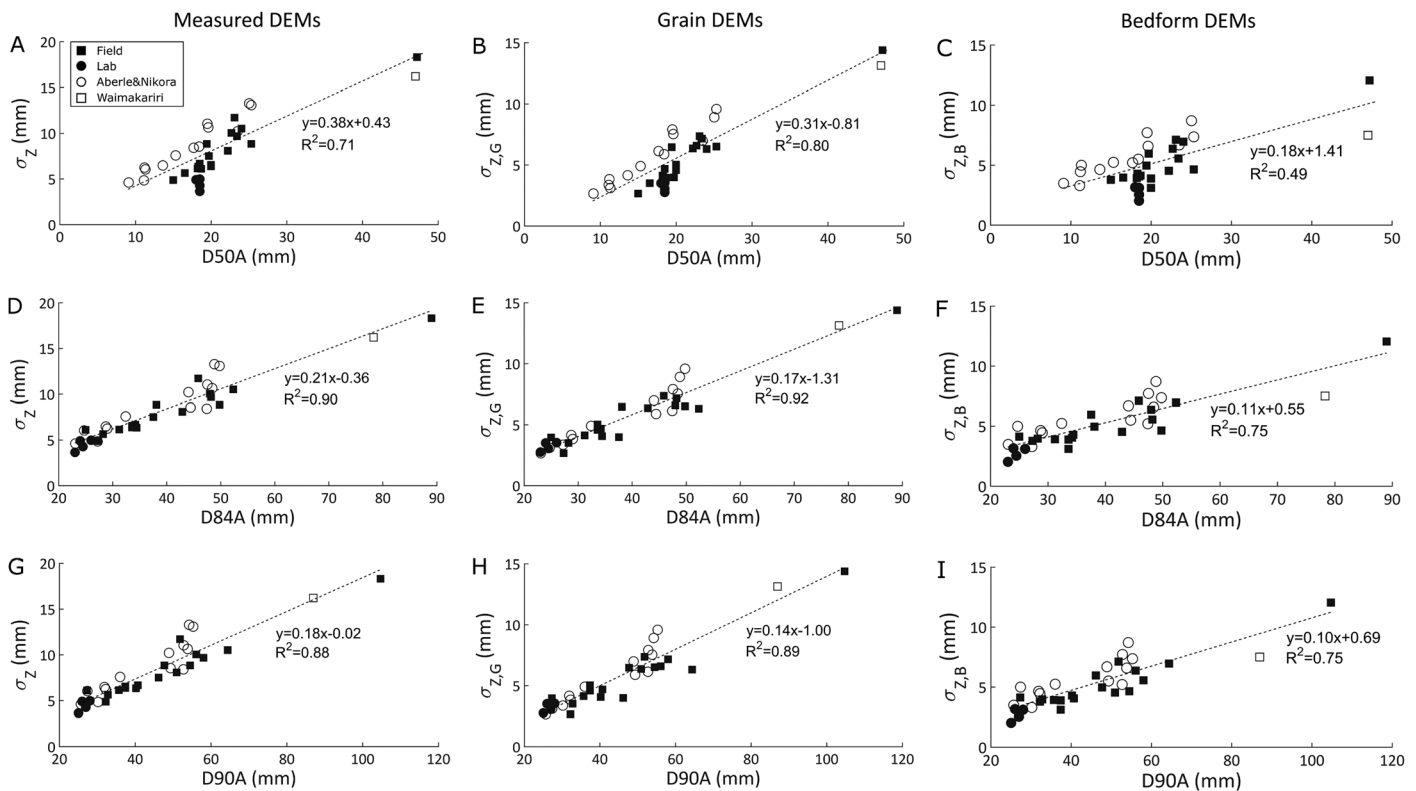


Figure 3. Relationships between the standard deviation of bed elevations (σ_z , $\sigma_{z,G}$, and $\sigma_{z,B}$), representing vertical roughness, determined from (a, d, g) the measured DEMs, (b, e, h) the grain DEMs, and (c, f, i) the bedform DEMs, respectively, and characteristic grain sizes (D_{50A} , D_{84A} , and D_{90A}) of the bed-surface material. Functional lines (i.e., corrected least squares lines) best representing the data are based on the 35 DEMs available. Closed symbols represent data collected by the authors, while open symbols represent data collected by others and made available to the authors. Round symbols are the laboratory surfaces; square symbols the field surfaces.

three percentiles. The strongest relationship ($R^2 = 0.92$, $p < 0.01$) is between $\sigma_{z,G}$ and D_{84A} (Figure 3e). A difference in surface sediment size between patches is therefore a good explanation of the different grain topographies. Differences in bedform topography between patches (i.e., $\sigma_{z,B}$) are not explained as well by the models (Figures 3c, 3f, and 3i). Statistical testing of the similarity between relation coefficients shows a similar response of σ_z and $\sigma_{z,G}$ to changes in sediment size ($p < 0.01$), for each percentile. The relations with $\sigma_{z,B}$ differ, with a lower slope, compared to the relations with σ_z and $\sigma_{z,G}$. We do observe, however, consistent patterns in intercept values across the graphs, which suggests that surface sediment size exerts a systematic control over measured, grain, and bedform topographies.

The relationships developed in Figure 3 were directly helpful to examine the connections between bedform geometry and the size of the bed-surface material. The assertion stated earlier, which is supported in consideration of bedform stability, is that surface sediment is coarser on bedform tops and finer in bedform troughs (Figure 1). For all 35 gravel patches, the bedform DEMs were used to delineate regions pertaining to humps or hollows on the surface, corresponding to bedform elevations above 1 mm and below -1 mm, respectively. As a proxy of sediment size, $\sigma_{z,G}$ (i.e., using the grain DEMs) was measured for humps and hollows separately, and the relationship presented in Figure 3e ($\sigma_{z,G} = 0.17D_{84A} - 1.31$, $R^2 = 0.92$) provided estimates of D_{84A} . Inversion of the equation to estimate D_{84A} from $\sigma_{z,G}$ was suitable due to the equation being a functional relationship [Mark and Church, 1977]. Figure 4a confirms that sediment is coarser on bedform tops (i.e., humps) and finer in the troughs (i.e., hollows). Given the form of the relations in Figure 3, using other percentiles than D_{84A} leads to the same findings. As shown in Table 1, the sorting of sediment size on the surface layer is accentuated for the field patches and the laboratory patches with high formative discharges. Separate analysis of the laboratory data for which formative flow conditions are known (Figure 4b) shows that the ratio of D_{84A} between humps and hollows (D_{hu}/D_{ho}) increases significantly with both formative discharge and Shields stress increases ($R^2 = 0.91$ for both relations, $p < 0.01$). Only two patches, corresponding to the experimental beds collected by the authors with Sed2 for which the Shields stresses based

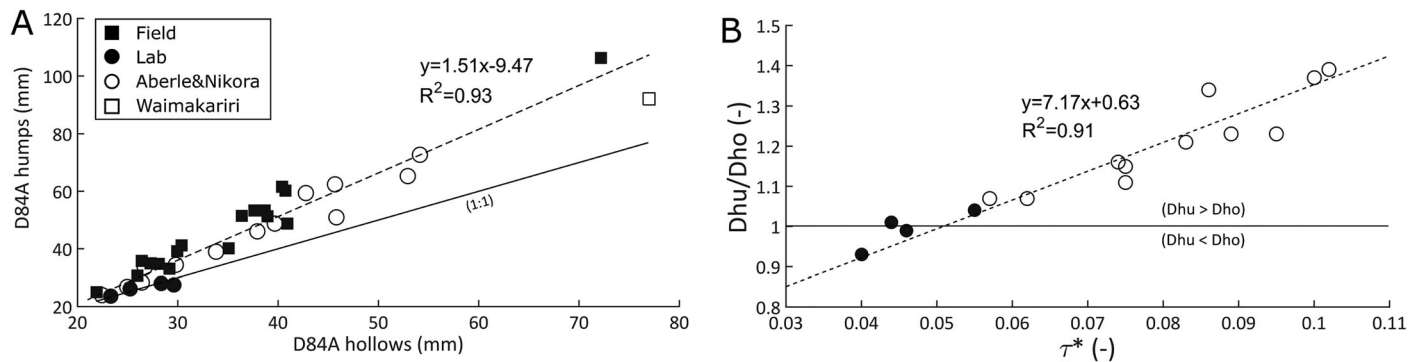


Figure 4. (a) Relationship between surface sediment size (D_{84A}) measured on bedform tops (humps) and bedform troughs (hollows) separately, for the 35 patches. Surface humps and hollows were isolated using the bedform DEMs, corresponding to bedform elevations above +1 mm and below -1 mm, respectively. The functional relationship developed in Figure 3e provided estimates of D_{84A} for bedform tops and troughs separately. Solid line illustrates 1:1 relationship. (b) Relationship between the ratio of D_{84A} measured on humps and hollows and the formative Shields stress for patches formed in a laboratory flume ($n = 15$, see Table 1).

on D_{50} were small ($\tau^* = 0.040$ and 0.046 , respectively), did not verify the assertion of coarse sediment on bedform tops and finer sediment in bedform troughs (Figure 4 and Table 1).

In Figure 5, we analyze how grain and bedform topographies isolated from DEMs relate to each other. Measured gravel-bed topography evolves collectively with the topography due to grain arrangements and the underlying bed undulations. σ_z is strongly correlated to both $\sigma_{z,G}$ measured from the grain DEMs ($R^2 = 0.96$) and $\sigma_{z,B}$ measured from the bedform DEMs ($R^2 = 0.89$). However, the two roughness scales have different relation coefficients ($p < 0.05$) when it comes to their imprint on the measured patch topography. Across most gravel patches in this study (Table 1) we observed that bedform roughness has a lesser impact on measured σ_z (i.e., $\sigma_{z,B}$ is smaller than $\sigma_{z,G}$). Based on the results presented in Figure 5, and assuming equal weight is given to the grain and the bedform function, a general relationship of the form $\sigma_z = 0.71\sigma_{z,G} + 0.82\sigma_{z,B}$ (mean residual error = 0.31 mm) appears to correctly represent gravel-bed vertical roughness embodied in patch-scale DEMs available for this study.

3.4. Effect of Roughness Scale Separation on Other Roughness Parameters

Figure 6 presents results on the inclination index measured in a direction parallel to the surface-forming flow direction, $I(0^\circ)$, for the same selection of four DEMs presented earlier. Similar to the results obtained with σ_z (Figure 2), the moving-window analysis technique shows that $I(0^\circ)$ has a wider range when measured over the bedform DEMs, suggesting large variability within a patch. Three patches show negative $I(0^\circ)$ values for the bedforms (Figures 6a, 6c, and 6d). This indicates the predominance of negative slopes, and because planar trends were removed suggests the existence of asymmetric bedforms with short-crested humps, and longer hollows. One gravel patch (Figure 6b) shows the opposite tendency. Measures of $I(0^\circ)$ for the grain DEMs have robust values and little variability at square window sizes as small as $(10D_{50A})^2$. Positive $I(0^\circ)$ for the grain DEMs suggests the predominance of positive DEM cell slopes, which is characteristic

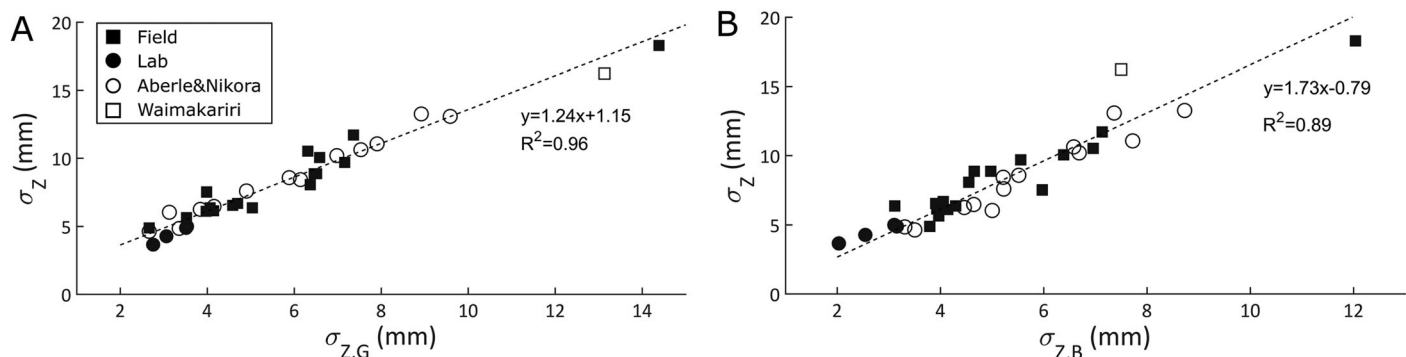


Figure 5. Relationships between the standard deviation of bed elevations (σ_z) determined from the measured DEMs and the standard deviation of bed elevations determined from (a) the grain DEMs ($\sigma_{z,G}$), and (b) the bedform DEMs ($\sigma_{z,B}$). The functional lines best representing the data are based on the 35 DEMs available.

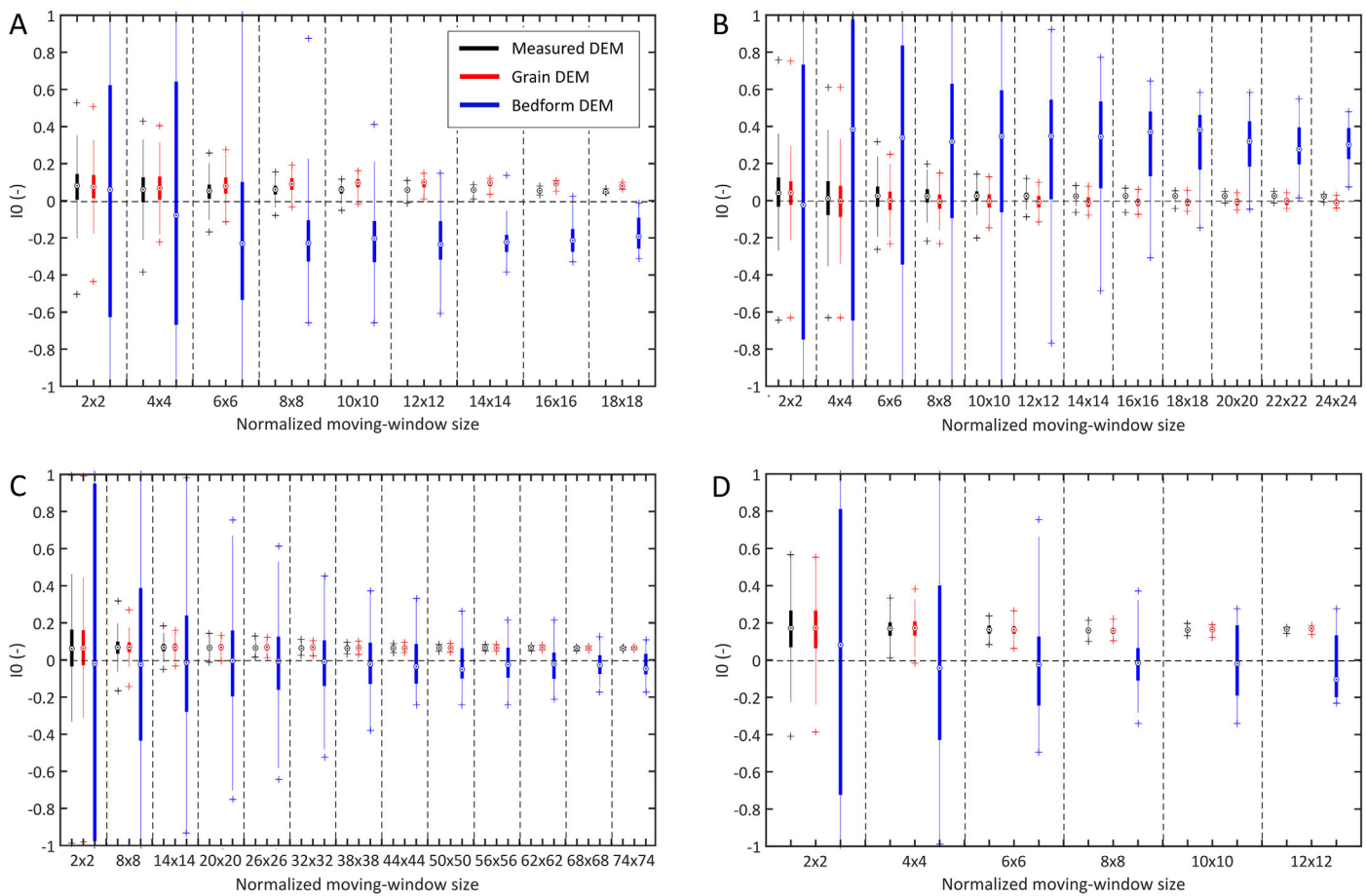


Figure 6. Moving-window analysis examining the spatial variations in inclination index along the flow direction, $I(0^\circ)$, for the same DEMs as presented in Figure 2 ((a) Sed1_Q2; (b) B1P11; (c) IV_Qc120; (d) Waimakariri). X axis is moving-window size normalized in both directions by D_{50A} . Boxplot coding same as Figure 2.

of grain imbrication [Millane *et al.*, 2006]. Measured DEMs, which combine grain and bedform topographies, show slightly different inclination indices compared to the grain DEMs with more variability at similar DEM sizes, because of the influence of bed undulations on DEM cells' slope.

Contour plots of second-order 2-D structure functions (called isopleth maps) are presented in Figure 7. Results focus on the two DEMs collected by the authors presented in Figure 1. Comparison can be made with the isopleth maps for the patches collected by Aberle and Nikora [2006] and presented in their paper (see their Figure 6). The analysis presented herewith and the observations drawn can be applied to the other patches.

Bed-elevation structure functions are inversely related to bed-elevation correlations. Regions in the middle of the isopleths with low structure function values represent the spatial lags at which bed elevations are correlated, generally because compared elevations lie on a same sediment grain or same bedform [Marion *et al.*, 2003]. Using 2-D structure functions, one can verify that bedform topography isolated with detrending (e.g., Figures 1e and 1f) is representative. Here it is clear that bed-elevation correlations at scales larger than the grain scale identified in the measured DEMs (Figures 7a and 7b) are correctly repeated in the bedform DEMs (Figures 7e and 7f). The irregular small-scale grain topography also shows through in the isopleth maps (Figures 7c and 7d).

The lag at which grain elevations are not correlated anymore (indicated by structure function values reaching the saturation level) appears to relate to the size of the bed-surface material (e.g., D_{50A}). Compared to the grain DEMs, elevation correlations for the measured and bedform DEMs decrease more slowly, but eventually, they also cancel out at sufficiently large lags. Observed in Figure 7 at small spatial lags (l_x and $l_y < 5D_{50A}$), the drop in bed-elevation correlation is not isotropic. That is, correlations hold longer in one

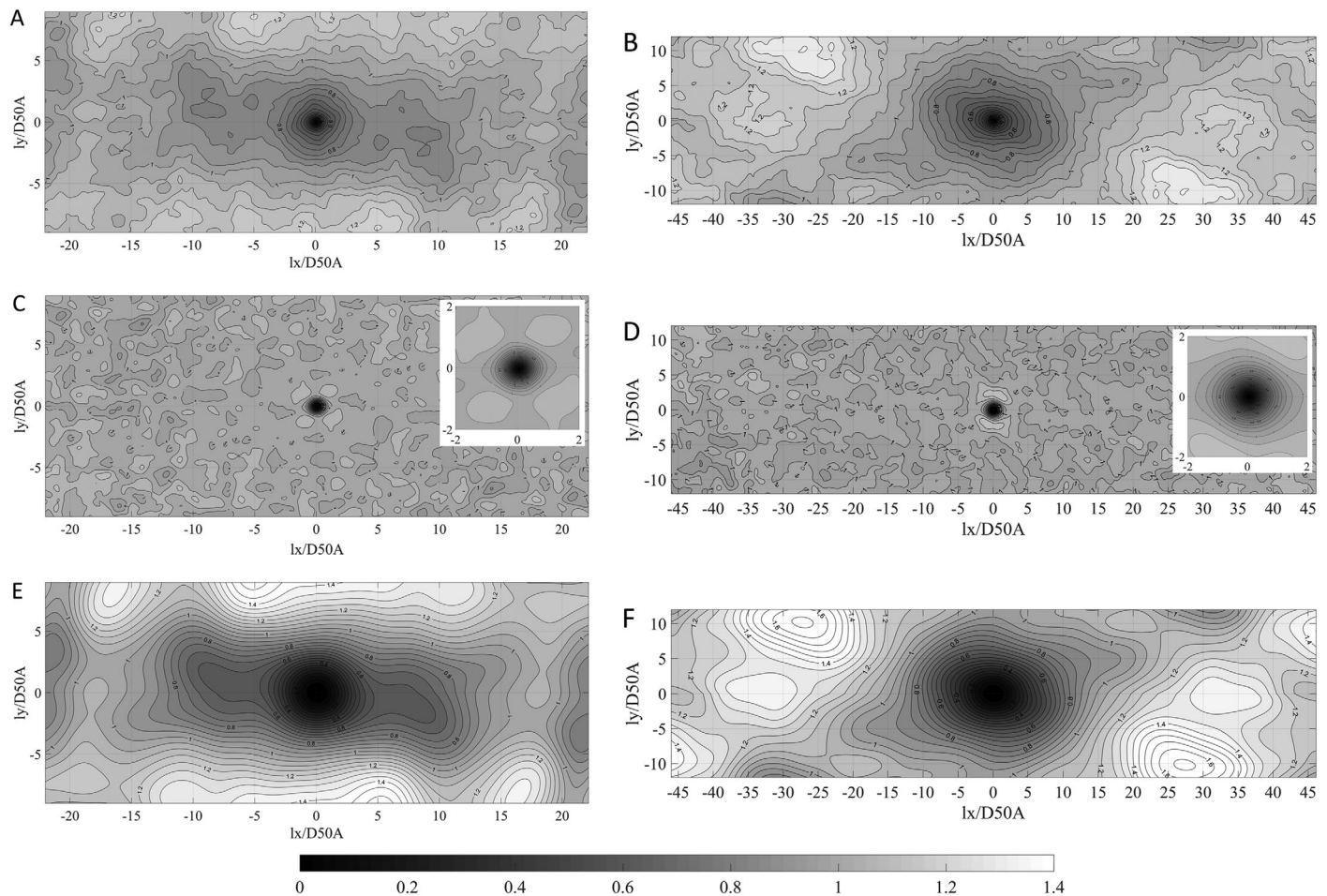


Figure 7. Second-order 2-D structure functions of bed elevations (isopleth maps), for the same DEMs as presented in Figure 1 ((a, c, e) Sed1_Q2; (b, d, f) B1P11). (a, b) First row corresponds to the measured DEMs; (c, d) second row to the grain DEMs; and (e, f) third row to the bedform DEMs. Colors are coded according to structure function values (i.e., inverse to bed-elevation correlations), normalized by the saturation level (equal to two-times the variance in elevations). To assist in the analysis, horizontal distances in the flow and transverse directions (l_x and l_y , respectively) were normalized by the bed-surface material D_{50A} .

direction, which can be representative of the general grain orientation when measured over the grain DEMs, or the general orientation of the bed undulations when applied to the bedform DEMs. For the grain DEMs (Figures 7c and 7d), the shape of the ellipses suggests a small predominance of grains at rest on the surface with their long axis parallel to the flow direction. Analysis of grain orientation with Basegrain[®], a Matlab toolbox for semiautomatic sediment grain detection and grain geometry analysis from digital images of the bed surface [Detert and Weitbrecht, 2012], showed the same tendency in that the proportion of grains aligned parallel to the flow was above that for other grain orientations.

Bed-elevation correlations for the bedform DEMs extend over larger lags. This echoes previous observations showing the need for larger window sizes to characterize bedform topography (Figures 2 and 6), compared to the grain topography. At lags approximately 20–25 D_{50A} , a subsequent increase in bed-elevation correlation is observed, suggesting the start of another bedform. This also indicates that the maximum lags used for computing structure functions (hence patch size) were too small to observe more than one bedform for these patches. The different shapes depicted in Figures 7e and 7f suggest different arrangements of the bedforms for the two patches presented, which is supported by visual observations of the DEMs (Figure 1).

Structure functions applied to the measured DEMs (Figures 7a and 7b) are harder to interpret due to the superposition of two distinct topographic signatures, one due to sediment grains, the other due to underlying bed undulations. Hence, it is difficult to separate the relative effect of both topographies and their characteristics.

4. Discussion

4.1. Isolating Roughness Scales From DEMs

A similar detrending method was used by *Powell et al.* [2016] to separate grain and bedform roughness scales from DEMs in their study on gravel-bed armors. Bedform DEMs (called mesoscale topography) were obtained using the method of regional-residual separation (RRS) by smoothing measured DEMs with a 100 mm boxcar filter. Likewise, grain DEMs were isolated by subtracting the bedform DEMs from the measured DEMs. The filter diameter of 100 mm approximated $3D_{84A}$ in their study (i.e., to approximately $2.75D_{90A}$, if it is assumed that $0.9D_{90A} = D_{84A}$). In this study, and similar to *Smart et al.* [2002], the filter diameter was set to $2.5D_{90A}$.

We investigated the effect of varying the filter diameter during detrending. Using a filter width of $2.75D_{90A}$ [*Powell et al.*, 2016] did not impact isolated topographies presented in Figure 1, and the relationships developed (as in Figures 3 and 5) were consistent with the ones obtained with a filter width of $2.5D_{90A}$. Increases in filter width above $3D_{90A}$ prevented effective roughness scale separation from DEMs. For instance, the resulting bedform DEMs did not support visual observations of humps and hollows present on the measured DEMs. Besides, correlations between roughness scales (Figure 5) and correlations between σ_z and sediment size (Figure 3) decreased. Finally, bedform shape was found to be unrealistic using 2-D structure functions. Similar to using too large filter diameters, detrending DEMs using a filter width below $2D_{90A}$ did not correctly pick up bed undulations present on the surface. This analysis highlights the importance of the filter diameter used for separating roughness scales from DEMs, and the need to confirm isolated topographies (i.e., grain and bedform DEMs) with visual observations made on the measured surfaces when possible [*Powell et al.*, 2016]. Based on the results we present, the observation of a strong relationship between roughness scales (e.g., as in Figure 5) may be used to assess the effectiveness of grain and bedform roughness separation from DEMs in future studies.

Using a moving-window analysis technique we showed that roughness scales identified in this study have different spatial signatures. Grain roughness parameters were robustly measured from (grain) DEMs when window hence patch size was over $\sim 12\text{--}18D_{50A}$ in both directions. This is shown in Figures 2 and 6 by consistent $\sigma_{z,G}$ and $l(0^\circ)$ with square window size increases above $\sim (12\text{--}18D_{50A})^2$. For DEMs smaller than this size, measures of grain roughness derived may not be representative of the surface due to the inherent spatial variability in grain topography (Figures 2 and 6), which in turn reflects complex grain arrangements as a result of water-working. The "Waimakariri [*Smart et al.*, 2004]" and "Field 2" gravel patches are the roughest surfaces (in terms of $\sigma_{z,G}$) we examined (Table 1). They are also the patches with the smallest normalized DEM size (13×13 and 19×13 for Waimakariri and Field 2, respectively). This may have impeded effective roughness characterization, eventually resulting in a slight deviation from the relationship developed for the complete data set (Figure 5a). To capture robust measures of bedform roughness, measurements need to cover even larger areas than is necessary for grain roughness [*Powell et al.*, 2016]. Figures 1, 7e and 7f all show that the gravel patches presented contained only a small number of humps and hollows on the surface. This may have affected $\sigma_{z,B}$ measured from the bedform DEMs and may explain increase in scatter between σ_z and $\sigma_{z,B}$ for the roughest surfaces (e.g., the Waimakariri DEM) analyzed in this study (Figure 5b). The assertion is further demonstrated in Figure 2, as $\sigma_{z,B}$ did not reach stable values even at the largest window sizes. Results in Figure 2 are based on four DEMs, which comprise gravel patches from all sources available and cover the largest range of sediment size allowed by our data set (Table 1). Thus, the representativeness of the selection is maximized. Currently, obtaining DEMs at a size and resolution allowing the measurement of several bed undulations and accurate characterization of grain topography, respectively, is still unprecedented. This is because of obvious challenges in efficient and effective data collection and handling. Future work may evaluate the possibility to use centimeter-scale DEMs (compared to using millimeter-scale DEMs as in this study), which are easier to collect over large areas with either photogrammetric or laser technologies, to answer questions on bedform spatial variability and the minimum patch size to measure bedform roughness signature. The moving-window analysis technique presented in this study may prove helpful for the analysis.

4.2. Implications for Roughness Parameterization Using Patch-Scale DEMs

The size of the coarse sediment at the surface (e.g., represented by D_{84A}) has a marked influence on surface vertical roughness represented by σ_z (Figure 3), which supports previous observations of the accentuated

effect of coarse sediment on gravel-bed structure and topography [e.g., Church *et al.*, 1998; Piedra *et al.*, 2012], compared to the smaller grains. Particularly, data from Figure 3 suggest that the size of the bed-surface material has a stronger influence on the isolated grain topography, and less on the underlying bed undulations ($R^2 = 0.92$ and $R^2 = 0.75$, between D_{84A} and $\sigma_{z,G}$, and between D_{84A} and $\sigma_{z,B}$, respectively). As a general observation, a gravel-bed surface made of fine sediment does not create as rough a surface as when it comprised coarse sediment. This can be explained by coarse sediment naturally protruding higher, and coarse particles being essential to the formation of cluster microforms [Brayshaw, 1985; Heays *et al.*, 2014] and stone cells [Church *et al.*, 1998], which increase surface variability and roughness. Results of this study show that coarse sediment also controls bedform geometry, with evidence of groupings of coarse particles forming humps on the surface, and finer sediment sheltered in hollows (Figures 1 and 4). This size-selective arrangement of the sediment on the surface layer was most marked for the field surfaces and the experimental surfaces formed at high Shields stress (Table 1 and Figure 4b), which certainly indicates a disposition for gravel beds to form grain structures in these conditions. We believe our findings are interesting to explain bedform formation and stability in gravel-bed streams. This also sheds light on the complex mechanisms involved during streambed armoring. For instance, relations between surface sediment size and grain and bedform roughness developed in this study, together with previous demonstrations of vertical roughness increases with formative discharge [Aberle and Nikora, 2006], support the assumption that grain and bedform roughness evolve in tandem with a coarse surface layer during armoring [Powell *et al.*, 2016]. Although no attempt was made to identify grain structures (e.g., clusters), partly because of the difficulty of an automatic and objective identification [Heays *et al.*, 2014], our results suggest a relation exists between the bedforms measured in this work and small-scale grain structures.

It is generally accepted that accounting for grain-scale roughness is critical for reliable characterization of bulk flow properties and turbulence in flow simulations over rough beds [Hardy *et al.*, 2009], with simulations increasingly making use of DEMs. For the DEMs studied, surface vertical roughness represented by σ_z was strongly controlled by the roughness due to the grains and bedforms taken separately (Figure 5). Based on our extensive data set of field and laboratory water-worked gravel beds, and strong relationships evidenced between roughness scales, it is conceivable that realistic measures of (ensemble) vertical roughness embodied in patch-scale DEMs can be obtained from knowing either grain or bedform vertical roughness. This means that lower-resolution DEMs, essentially measuring the larger features such as bedforms, but not detailed enough for grain roughness characterization, may be used to infer grain roughness and the vertical roughness of a gravel patch. Likewise, flow modeling studies using cruder DEMs [e.g., Casas *et al.*, 2010] for the sake of meaningful computational domains yet time-efficient computations, may use results presented in this work to reconstruct (or parameterize) gravel-bed microtopography from the smoothed bed topography available. We believe the relationships we obtained for roughness scales are an important step in advancing our roughness parameterization understanding.

The effect of separating roughness scales was assessed on other DEM properties such as the inclination index in the flow direction, $I(0^\circ)$. Figure 6 shows that characterization of grain imbrication with $I(0^\circ)$ is facilitated when using the grain DEMs, with consistent values obtained at square window sizes over $\sim(12-16D_{50A})^2$, which is similar to previous observations made on σ_z (Figure 2). If $I(0^\circ)$ is estimated from the measured DEMs, slopes due to the underlying bed undulations may blur the effect of grains on the predominance of positive DEM cell slopes. Although not suitable for measuring grain imbrication, $I(0^\circ)$ determined from bedform DEMs identifies general bedform inclination and shape, which, as in the case of sand-bed rivers, may be relevant parameters for form resistance [Chie Yen, 2002].

Analysis of bed-elevation structure functions has also profited from the prior separation of grain and bedform topographies. Previous research showed that structure functions (or equivalent semivariograms) allow for the determination of various scales of roughness from measurements of surface topography [Robert, 1988, 1991; Butler *et al.*, 2001]. Correlation lengths for the different scales of roughness are estimated as the spatial lags at which elevations are not correlated anymore. However, when applied to measured DEMs encompassing both grain and bedform topographies, 2-D bed-elevation structure functions were hard to interpret and attributing correlation lengths to roughness scales was found to be quite subjective, as evidenced in Figures 7a and 7b. Another classic method to determine horizontal correlation lengths of river-bed topography, although generally limited to either along flow or transverse flow directions, is to plot 1-D profiles of structure functions and to use power functions fitted to the scaling region at small lags [e.g.,

Robert, 1991]. Initial research using 1-D transects of gravel-bed elevations suggested the existence of at least two scaling regions. However, recent work using more detailed and areal laser scans of gravel-bed surfaces found this method of analysis ambiguous, which did not allow effective roughness scale separation [Hodge *et al.*, 2009]. The work presented herein shows the relevance of using moving-window detrending prior to structure functions analysis, as this allows separate investigations of bed-elevation correlations for the grain and bedform topographies (see Figure 7). Hence, characteristics of each topographic signature (i.e., either grain or bedform) such as correlation length and general spatial arrangement can be readily gathered from isopleth maps. An example analysis was presented for two DEMs collected by the authors.

Previous work investigated relations between flow resistance and bed roughness for gravel-bed rivers. Bed roughness was initially related to sediment size (e.g., $k_s = 3.5D_{84A}$). The effect due to the surface sediment grains was accounted for explicitly, however required a multiplier to account for larger-scale roughness effect on flow resistance attributed to the occurrence of cluster microforms [Clifford *et al.*, 1992]. A similar effort was made by Millar [1999] to explain the roughness multiplier. Respective contributions of grain and form resistance for 176 gravel reaches were compared and it was concluded that form resistance due to gravel bars and pool-riffle sequences can have a significant effect on total flow resistance [Millar, 1999]. Compared to grain roughness, the absence of predictive relations for form resistance was deplored. Results presented herein, which relate bedform roughness of gravel patches to grain roughness and sediment size, contribute to filling this gap. Besides flow resistance modeling, roughness partitioning (similar separation can be applied to the shear stress and friction coefficient) has been suggested also as a means to enhance our understanding of sediment transport mechanisms in alluvial rivers [e.g., Chie Yen, 2002]. For instance, an estimate of initial sediment movement requires separate evaluation of the shear stress applied to the grains, as in the event of bedload transport the latter represents the effective flow contribution [Robert, 1988]. The novelty in this study is the ability to isolate roughness scales from measurements of the bed topography. This way, distinct roughness signatures can be determined and linked to observations of bed topography. This discussion has presented the potential contributions this can make to advance our present understanding of the intricate relations between the sediment bed, flow resistance and sediment transport.

5. Conclusion

Modern techniques now allow detailed measurement and analysis of water-worked gravel-bed topography. This has led to a resurgence of studies on the controls of bed topography over flow and sediment transport in gravel-bed rivers. High-resolution DEMs are well suited to relate roughness parameters to gravel-bed topographies. Although roughness is scale-dependent, traditionally, methods to determine roughness scales and to isolate roughness effects have been limited to using structure functions of bed elevations—an analysis technique which has been found to have limitations when dealing with complex surfaces such as gravel patches.

This study has used a moving-window detrending technique to examine roughness scale isolation from patch-scale gravel-bed DEMs. An extensive data set comprising 35 water-worked gravel surfaces of varying size and resolution, collected in either a laboratory flume or the field, was used for the analysis. It has been shown that provided attention is given to the filter width used for detrending, it is possible to isolate the respective topographies relating to sediment grains and the underlying small bedforms, respectively. Hence, roughness properties of the sediment grains and bedforms can be measured separately and related to the scale of measurement. The results demonstrate that measures of grain roughness are easier to determine at smaller DEM sizes than bedform roughness signatures, which requires larger DEM size. Grain vertical roughness is associated with the size of the coarse sediment forming the bed surface. Coarse sediment also controls bed undulations (bedforms) by forming humps on the surface, in the lee of which finer sediment is sheltered. Finally, we showed that patch-scale vertical roughness represented by σ_z can be estimated by knowing either grain vertical roughness or bedform vertical roughness (relationships presented in Figure 5). This is an important finding for two reasons. First, it provides an opportunity for flow modelers to parameterize gravel-bed microtopography from the smoothed beds used as input surfaces, helping to obtain realistic findings on flow variability and turbulence. Second, it provides new means to compare measures of surface roughness (here σ_z) found in the literature, which were obtained using different detrending techniques. There is also potential to apply the technique presented for quantifying small-scale grain

structures, such as clusters. Important work remains to be done linking bed topography and flow properties in gravel-bed rivers. The combined use of topography and flow remote sensing may ultimately allow realistic characterization of the topographic controls on flow resistance.

Acknowledgments

The analysis was partly undertaken using a High-Performance Computing (HPC) platform provided by the New Zealand eScience Infrastructure (NeSI). The study was supported by the Marsden Fund (grant UOA1412) administered by the Royal Society of New Zealand. The authors are grateful to Jochen Aberle, Graeme Smart, and Rick Millane for making data available and acknowledge the constructive comments of Michael Church and two anonymous reviewers. The digital elevation models analyzed in this study are archived at the University of Auckland and are freely available from the lead author upon request.

References

- Aberle, J., and V. Nikora (2006), Statistical properties of armored gravel bed surfaces, *Water Resour. Res.*, 42, W11414, doi:10.1029/2005WR004674.
- Aberle, J., and G. M. Smart (2003), The influence of roughness structure on flow resistance on steep slopes, *J. Hydraul. Res.*, 41(3), 259–269.
- Bertin, S., and H. Friedrich (2016), Field application of close-range digital photogrammetry (CRDP) for grain-scale fluvial morphology studies, *Earth Surf. Process. Landforms*, 41, 1358–1369.
- Bertin, S., H. Friedrich, P. Delmas, E. Chan, and G. Gimelfarb (2014), DEM quality assessment with a 3D printed gravel bed applied to stereo photogrammetry, *Photogramm. Rec.*, 29(146), 241–264.
- Bertin, S., H. Friedrich, P. Delmas, E. Chan, and G. Gimelfarb (2015), Digital stereo photogrammetry for grain-scale monitoring of fluvial surfaces: Error evaluation and workflow optimisation, *ISPRS J. Photogramm. Remote Sens.*, 101, 193–208.
- Bertin, S., H. Friedrich, and P. Delmas (2016), A merging solution for close-range DEMs to optimize surface coverage and measurement resolution, *Photogram. Eng. Remote Sens.*, 82(1), 31–40.
- Bouquet, J.-Y. (2010), Camera calibration toolbox for Matlab, Caltech, Pasadena, Calif. [Available at http://www.vision.caltech.edu/bouquetj/calib_doc/]
- Brayshaw, A. (1985), Bed microtopography and entrainment thresholds in gravel bed rivers, *Geol. Soc. Am. Bull.*, 96(2), 218–223.
- Butler, J. B., S. N. Lane, and J. H. Chandler (2001), Characterization of the structure of river-bed gravels using two-dimensional fractal analysis, *Math. Geol.*, 33(3), 301–330.
- Casas, M. A., S. N. Lane, R. J. Hardy, G. Benito, and P. J. Whiting (2010), Reconstruction of subgrid-scale topographic variability and its effect upon the spatial structure of three-dimensional river flow, *Water Resour. Res.*, 46, W03519, doi:10.1029/2009WR007756.
- Chie Yen, B. (2002), Open channel flow resistance, *J. Hydraul. Eng.*, 128(1), 20.
- Church, M., M. A. Hassan, and J. F. Wolcott (1998), Stabilizing self-organized structures in gravel-bed stream channels: Field and experimental observations, *Water Resour. Res.*, 34(11), 3169–3179.
- Clifford, N., A. Robert, and K. Richards (1992), Estimation of flow resistance in gravel-bedded rivers a physical explanation of the multiplier of roughness length, *Earth Surf. Process. Landforms*, 17(2), 111–126.
- Coleman, S. E., V. I. Nikora, and J. Aberle (2011), Interpretation of alluvial beds through bed-elevation distribution moments, *Water Resour. Res.*, 47, W11505, doi:10.1029/2011WR010672.
- Detert, M., and V. Weitbrecht (2012), Automatic object detection to analyze the geometry of gravel grains, paper presented at RiverFlow 2012, Taylor and Francis Group, San Jose, Costa Rica.
- Fehr, R. (1987), *Geschiebeanalysen in Gebirgsflüssen translated Analysis of Sedimentary Bed Material in Mountain Rivers. Conversion and Comparison of Various Analytical Methods*, Nr. 92, Mitt. der Versuchsanstalt für Wasserbau, Hydrol. und Glaziol., Eidg. Tech. Hochsch., Zürich.
- Folk, R. L., and W. C. Ward (1957), Brazos River bar [Texas]; a study in the significance of grain size parameters, *J. Sediment. Res.*, 27(1), 3–26.
- Gimelfarb, G. (2002), Probabilistic regularisation and symmetry in binocular dynamic programming stereo, *Pattern Recogn. Lett.*, 23(4), 431–442.
- Graham, D. J., A. J. Rollet, H. Piégay, and S. P. Rice (2010), Maximizing the accuracy of image-based surface sediment sampling techniques, *Water Resour. Res.*, 46, W02508, doi:10.1029/2008WR006940.
- Griffiths, G. A. (1989), Form resistance in gravel channels with mobile beds, *J. Hydraul. Eng.*, 115(3), 340–355.
- Hardy, R. J., J. L. Best, S. N. Lane, and P. E. Carbonneau (2009), Coherent flow structures in a depth-limited flow over a gravel surface: The role of near-bed turbulence and influence of Reynolds number, *J. Geophys. Res.*, 114, F01003, doi:10.1029/2007JF000970.
- Heays, K. G., H. Friedrich, and B. W. Melville (2014), Laboratory study of gravel-bed cluster formation and disintegration, *Water Resour. Res.*, 50, 2227–2241, doi:10.1002/2013WR014208.
- Hey, R. D. (1988), Bar form resistance in gravel-bed rivers, *J. Hydraul. Eng.*, 114(12), 1498–1508.
- Hodge, R., J. Brasington, and K. Richards (2009), Analysing laser scanned digital terrain models of gravel bed surfaces: Linking morphology to sediment transport processes and hydraulics, *Sedimentology*, 56(7), 2024–2043.
- Kirchner, J. W., W. E. Dietrich, F. Iseya, and H. Ikeda (1990), The variability of critical shear stress, friction angle, and grain protrusion in waterworked sediments, *Sedimentology*, 37(4), 647–672.
- Lane, S., J. Chandler, and K. Porfiri (2001), Monitoring river channel and flume surfaces with digital photogrammetry, *J. Hydraul. Eng.*, 127(10), 871–877.
- Lane, S. N., R. J. Hardy, L. Elliott, and D. B. Ingham (2002), High-resolution numerical modelling of three-dimensional flows over complex river bed topography, *Hydrol. Processes*, 16(11), 2261–2272.
- Laronne, J. B., and M. A. Carson (1976), Interrelationships between bed morphology and bed-material transport for a small, gravel-bed channel, *Sedimentology*, 23(1), 67–85.
- Marion, A., S. J. Tait, and I. K. McEwan (2003), Analysis of small-scale gravel bed topography during armoring, *Water Resour. Res.*, 39(12), 1334, doi:10.1029/2003WR002367.
- Mark, D. M., and M. Church (1977), On the misuse of regression in earth science, *Math. Geol.*, 9(1), 63–75.
- Millane, R. P., M. I. Weir, and G. M. Smart (2006), Automated analysis of imbrication and flow direction in alluvial sediments using laser-scan data, *J. Sediment. Res.*, 76(8), 1049–1055.
- Millar, R. G. (1999), Grain and form resistance in gravel-bed rivers, *J. Hydraul. Res.*, 37(3), 303–312.
- Nikora, V. I., D. G. Goring, and B. J. F. Biggs (1998), On gravel-bed roughness characterization, *Water Resour. Res.*, 34(3), 517–527.
- Noss, C., and A. Lorke (2016), Roughness, resistance, and dispersion: Relationships in small streams, *Water Resour. Res.*, 52, 2802–2821, doi:10.1002/2015WR017449.
- Pender, G., T. B. Hoey, C. Fuller, and I. K. McEwan (2001), Selective bedload transport during the degradation of a well sorted graded sediment bed, *J. Hydraul. Res.*, 39(3), 269–277.
- Piedra, M. M., H. Haynes, and T. B. Hoey (2012), The spatial distribution of coarse surface grains and the stability of gravel river beds, *Sedimentology*, 59(3), 1014–1029.
- Powell, D. M., A. Ockelford, S. P. Rice, J. K. Hillier, T. Nguyen, I. Reid, N. J. Tate, and D. Ackerley (2016), Structural properties of mobile armors formed at different flow strengths in gravel-bed rivers, *J. Geophys. Res. Earth Surf.*, 121, 1494–1515, doi:10.1002/2015JF003794.

- Robert, A. (1988), Statistical properties of sediment bed profiles in alluvial channels, *Math. Geol.*, 20(3), 205–225.
- Robert, A. (1991), Fractal properties of simulated bed profiles in coarse-grained channels, *Math. Geol.*, 23(3), 367–382.
- Scown, M. W., M. C. Thoms, and N. R. De Jager (2015), Measuring floodplain spatial patterns using continuous surface metrics at multiple scales, *Geomorphology*, 245, 87–101.
- Smart, G., M. Duncan, and J. Walsh (2002), Relatively rough flow resistance equations, *J. Hydraul. Eng.*, 128(6), 568–578.
- Smart, G., J. Aberle, M. Duncan, and J. Walsh (2004), Measurement and analysis of alluvial bed roughness, *J. Hydraul. Res.*, 42(3), 227–237.
- Tarolli, P. (2014), High-resolution topography for understanding Earth surface processes: Opportunities and challenges, *Geomorphology*, 216, 295–312.
- Wilcox, A. C., J. M. Nelson, and E. E. Wohl (2006), Flow resistance dynamics in step-pool channels: 2. Partitioning between grain, spill, and woody debris resistance, *Water Resour. Res.*, 42, W05418, doi:10.1029/2005WR004277.
- Zhang, Z. (1998), A flexible new technique for camera calibration, *IEEE Trans. Pattern Anal. Mach. Intell.*, 22(11), 1330–1334.